AIAA SciTech Forum
6-10 January 2020, Orlando, FL
AIAA Scitech 2020 Forum

10.2514/6.2020-1566

Experiment Integrated Numerical Modeling of a Channel Dielectric Barrier Discharge Plasma Actuator

Alexander J. Lilley[*], Lucas Z. Michels[†], and Subrata Roy[‡]
Applied Physics Research Group at the University of Florida, Gainesville, FL, 32611

There has been extensive numerical and experimental work done with surface mounted dielectric barrier discharge (DBD) actuators in the context of flow control and microfluidics. These actuators are quite limited in their energy conversion efficiency (0.1%) due to a large drag from the plasma induced Glauert-like wall jet. Contrarily, published experimental studies have shown that the channel DBD plasma actuators can achieve 700% higher efficiency than surface DBD actuators at the cost of not being flush mounted. The channel actuator can find use as a flow effector where flush mounting is not a concern, and conventional flow control techniques (e.g. flaps) are not well suited. Another possible use is for local cooling and/or ingestion where the housing is too small to physically incorporate a mechanical blowing mechanism. This paper introduces a basic numerical model for calculating the exponential electrostatic forcing function using the Poisson-Boltzmann equation. The forcing function is then used in the compressible FDL3DI code to predict the flow inducement inside the plasma channel. Time-averaged particle image velocimetry (PIV) is used to validate the numerical results. It was found that the forcing function predicted flow distribution quite similar to the experiment but estimated a slightly higher peak velocity (4.2 m/s versus 5 m/s). The computed channel exit velocity induced by the forcing function also matched with reported publications.

h_{ch} = channel height $[m]$
l_{ch} = channel length $[m]$
$\mathrm{U}_{\text{cl-Out}}$ = centerline velocity at channel outlet $[m/s]$
M_{Out} = centerline Mach number at channel outlet
t_d = dielectric thickness $[m]$
t_{ge} = ground electrode thickness $[\mu m]$
w = ground electrode length $[m]$
g = distance between electrode centers $[m]$
d_{wire} = wire diameter $[m]$
F_{x0} = x component of force scaling for model $[N]$
F_{y0} = y component of force scaling for model $[N]$
β = Decay constant related to material properties $[1/m]$
ϕ = peak applied potential $[kV]$
ϵ_0 = Permittivity of Air $[F/m]$
n_i = Number of ions
n_e = Number of electrons
e = The elementary charge $[C]$
x_0 = x location of actuator within domain $[m]$
y_0 = y location of actuator within domain $[m]$

---

[*] Graduate Research Assistant, Mechanical and Aerospace Department, AIAA Student Member
[†] Undergraduate Research Assistant, Mechanical and Aerospace Department, AIAA Student Member
[‡] Professor, Mechanical and Aerospace Department Associate Fellow

I. Introduction

As aerospace technology progresses, performance is expected to follow. From an aerodynamic perspective, flow control is a very attractive method of increasing performance of an aircraft, most importantly for drag reduction and stall delay. Various methods have been used for flow control, from flaps to vortex generators, each with their own advantages. Flow control is separated into two main areas, passive and active. Passive flow control devices do not require any external energy source. They allow for separation delay during high angle of attack maneuver, are very light, and are cost-effective. Unfortunately, they cannot be "turned off", even when their effect is not needed, hence has the drawback of unintended drag. In contrast, active flow control devices require external energy source and can become bulkier. However, active flow control devices control the surrounding flow only when necessary and otherwise can be "turned off". The drawbacks of active flow control are generally additional electronics complexity and power consumption. One active flow control method which has garnered interest in the past two decades is plasma actuators [1]. These actuators have potential use as light weight, surface compliant, and highly responsive for active flow control.

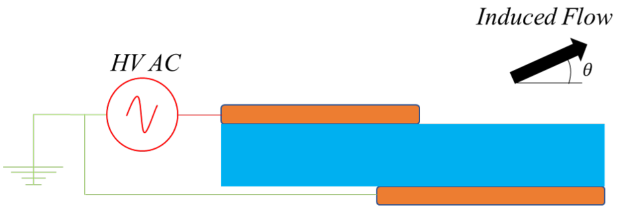

Fig. 1 Standard Surface Dielectric Barrier Discharge Plasma Actuator. Note the design can be surface mounted but the max force is applied near the wall.

Dielectric barrier discharge (DBD) plasma actuators function by applying alternating (on the order of kHz) high voltage (on the order of kV) between two electrodes that are separated by a dielectric medium as shown in Fig. 1. The resulting large electric field weakly ionizes the surrounding gas forming a net space charge. The charged particles are propelled with momentum from the electric field. These particles then collide with the neutral particles inducing a bulk flow near the actuator[2]. Because plasma actuators have no moving parts and can apply near instantaneous response, they can be used for high frequency applications where conventional mechanical active or passive flow control methods cannot. Plasma actuators do not require thick electrodes and therefore are very light but are much weaker in their fluidic coupling than their conventional mechanical counterparts. Research is ongoing in optimizing the placement, geometry and electrical input parameters of the plasma actuator for connecting to modes of high flow instability so as to amplify the effect of plasma actuators and thus their control authority.

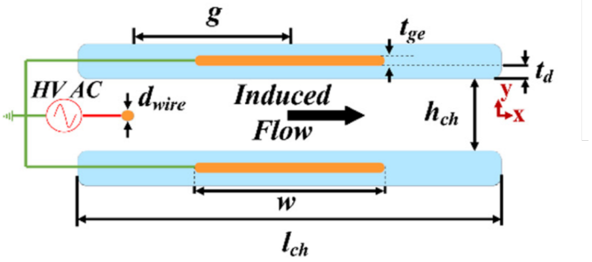

Fig. 2 Channel dielectric barrier discharge plasma actuator from Campbell and Roy [3]. By design the maximum force is applied far from the wall.

As the study of plasma actuator matures, various novel plasma actuators configurations and different designs have emerged. There has been significant study into linear [4][5] and serpentine actuators [6][7]. These design variations fall under the category of surface dielectric barrier discharge (SDBD) plasma actuators. It was found that the SDBD actuator is an effective method to pump fluid for large rectangular channels [8][9]. However, due to the induced wall shear by the SDBD, the energy conversion efficiency and outlet velocity of this channel are quite limiting [8]. In the case that it is permissible to mount a wire spanning the channel, the SDBD actuator can be converted into the channel dielectric barrier discharge (CDBD) actuator. The motivation to switch from SDBD to CDBD actuators is CDBD actuators were found to be 700% more efficient that SDBD actuators by Campbell and Roy [3].

The objective of this paper is to propose a numerically derived forcing function for the CDBD actuator that can be easily implemented for design considerations. The force is calculated by multiplying the Boltzmannian space charge and the electric field. The latter is found by solving the Poisson equation. An approximate forcing function is formulated to match the force distribution. This forcing function is then implemented into the compressible fluid solver FDL3DI [10] for predicting the resulting flow field inside the channel. Finally, to validate the numerical flow results, particle image velocimetry (PIV) experiment is performed on the interior of the channel actuator. The PIV is performed at 20,000 frames per second and a total of approximately 18,000 frames are averaged to produce a final result.

The paper is organized into five main sections. The Experiment section contains information on the setup and procedures for performing PIV within the channel actuator. The Poisson Equations section contains information on assumptions made, parameters used, and implementation details for finding the forcing function. The Numerical Simulation of Flow section contains information on FDl3DI, its schemes, and the grid used for the simulation of the flow. The Results section includes experimental results, Poisson equation solution, and flow simulation results inside the plasma channel. The Discussion section describes all results. Finally concluding remarks are drawn in the Conclusion section.

II. Experiment

A. Actuator Construction

The specifications used to design this actuator are given in Table 1 and are based on Campbell and Roy [3], except for the channel length. The channel length was reduced to 26.7 *mm* to aid observation of the laser sheet to collect PIV data from the inside of the channel. For lengths shorter than 26.7 *mm* destructive arcing occurred, which may be avoided with more robust materials. The wall of the channel nearest to the camera was hollowed out to avoid visual pollution. The height, h, of the inlet of the channel is 5 *mm*. The diameter of the copper wire is 203.2 μm. The distance between the center of the buried electrode and the wire, w, is 6.35 mm. The electrode copper electrode is 12.7 mm long and 70 µm thick as seen in fig 2. To ensure that plasma is not formed outside the channel the buried electrode is encapsulated in Kapton tape.

Table 1 Specifications of the Channel Actuator Tested

Parameter	Definition	Value
h_{ch}	Height of Channel	5.0 [mm]
l_{ch}	Length of Channel	26.7 [mm]
w_{ch}	Width of channel	100 [mm]
t_d	Dielectric thickness	2 [mm]
t_{ge}	Thickness of Cathode	70 [μm]
w	Cathode width	12.7 [mm]
g	Anode distance from center of Cathode	6.35 [mm]
d_{wire}	Diameter of Anode (wire)	0.2032 [mm]
f	Frequency of sinusoidal input signal	14 [Hz]
ϕ	Applied voltage	26 [kV]

B. Particle Image Velocimetry Setup

A 600 *mm* by 250 *mm* by 250 *mm* quiescent chamber was used to contain the channel actuator, laser, and seeding device. The entire setup is mounted on two Velmex BiSlides (computer controlled linear positioning devices) which were mounted to an optical table. A manually operated scissor lift is used to add another axis of mobility to the system as seen in fig 3. The Phantom v7.3 high speed camera was mounted to the same optical table to that the BiSlide was attached to. The Phantom v7.3 camera was used to perform instantaneous Particle Image Velocimetry (PIV). The experiment was performed at a resolution of 700 x 300 at 20,000 frames per second. Each PIV session yielded approximately 18,000 individual frames. The seeding was performed by atomizing Ondina oil with high pressured air to particle sizes between 1 and 5 μm. To illuminate the seeds, a 1 W blue laser (465 nm wave length) was used. A concave-convex lens is used to split the beam into a 10 degree plane. Because the laser is continuous, it was not necessary to setup a trigger to synchronize the camera and the laser.

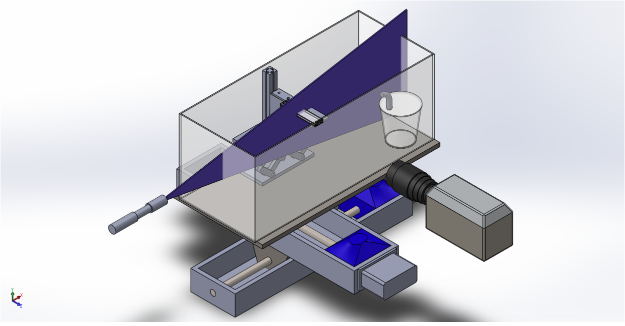

Fig. 3 Schematic of the particle image velocimetry setup. Note the computer controlled operators are used to control the horizontal axes. A manually operated scissor lift is used to adjust the vertical axis. The camera and laser are both fixed. The laser mounting system and top cover of the quiescent chamber are omitted for clarity.

C. Electronic Setup

A Tektronix arbitrary function generator (Model AFG3022B) was used as input to a series of amplifiers. The output of the function generator was passed through a QSC audio amplifier (Model RMX 2450) and finally through a custom amplifier. Due to high voltage, all wires were suspended using a plastic 3d printed carriage. To monitor the frequency and voltage of the actuator, a Tektronix DPO2014 oscilloscope was used. The actuator was run at a sinusoidal 14 kHz and 26 kV.

D. Data Processing

Each individual frame was passed through a 3 pixel by 3 pixel Hipass filter and saved as .tif file. The particle image velocimetry was performed in the MATLab program PIVlab [11]. The images were analyzed in a 1-2 2-3 3-4 configuration. Velocity vectors seven standard deviations (7 σ) or greater were considered spurious and removed. Points less than half a millimeter from the upper and lower wall were not considered to avoid clearly spurious vectors.

III. Poisson Equation

The Poisson-Boltzmann equation (1) was used to predict the electric field distribution considering the wire as the anode where the peak voltage was applied. The plate electrode embedded in the channel wall was considered as the ground. The electrostatic force was calculated by the product of electric field and separated space charge of the plasma. By only considering the Poisson equation the temporal terms and the magnetic field were assumed to be zero. These assumptions provide a rough estimate of the force distribution. The relevant symbols and the chosen values can be seen in Table 2.

The Poisson equation states the Laplacian of the potential field multiplied by the permittivity of air is equal to the difference in ions and electrons multiplied by the electronic charge (Eq. 1). The plasma is weakly (singly) ionized and therefore the ionicity factor Z is 1, meaning that an ion is formed by losing only one electron.

$$\epsilon_0 \nabla^2 \phi = e(n_e - Z n_i) \tag{1}$$

A. Physics of the Poisson Equation

In order to approximate right hand side of Eq. 1 the number density of ion (n_i) was assumed constant after the anode, except within 100 Debye length radius of the wire anode. Within the 100 Debye length radius, the distribution

Table 2 Parameters for the Poisson Equation

Symbol	Value	Value
L_{ch}	Channel X length	0.0267 $[m]$
H_{ch}	Channel Y length	0.005 $[m]$
ϕ_{max}	Maximum applied potential	26 $[kV]$
e	The elementary charge	1.602176634E-19 $[C]$
n_i	Ion density*	4E19 $[ions/m^3]$
n_e	Electron density	Variable $[electrons/m^3]$
$n_{e\infty}$	Electron density away from potential field	4.0E19 $[electrons/m^3]$
T_e	Electron temperature	3.0 $[eV]$
ϵ_0	Permittivity of Air	8.85E-12 $[F/m]$
Z	Degree of ionization	1
λ_D	Debye length	4E-6 $[m]$

*The number of ions 100 Debye lengths from the wire is a tenth of this value

of ions was assumed to be an order of magnitude less dense due to the strong positive charge of the anode. Electron distribution is considered Boltzmannian. Because the kinetic energy of the electron is much smaller than the potential energy, the Boltzmann factor was further approximated only using the electron temperature.

$$n_e \propto exp(-(mv^2/2 + e\phi)/T_e) \approx exp(-e\phi/T_e) \tag{2}$$

Where, T_e, the electron temperature is assumed constant. Next, plasma was assumed quasineutral at infinity, i.e., the number and distribution of electrons and ions are equal. This means that the electric field must be zero at infinity.

$$n_e = n_{e\infty} exp(-(e\phi)/T_e) \approx e^2 n_{e\infty}\phi/T_e \tag{3}$$

For small values of $-(e\phi)/T_e$ it was approximated as $e^2 n_{e\infty}\phi/T_e$ as seen in eq. 3. Finally, ϕ was treated as a constant at the anode with a radial exponential decay function, where the rate of decay is proportional to the radial distance, r, divided by the Debye length, λ_D, as seen in eq. 4.

$$\phi \propto exp(-r/\lambda_D) \tag{4}$$

The equation being numerically solved then becomes Eq. 5 where ϕ_{max} is the applied voltage at the electrode.

$$\nabla^2\phi = e^2 \frac{n_{e\infty}}{T_e\epsilon_0}\phi_{max} exp(-r/\lambda_D) - \frac{en_i}{\epsilon_0} \tag{5}$$

B. Numerical Procedure for Solution of Poisson Equation

The grid was evenly distributed in the x and y directions. The x direction contained a total of 200 points, while the y direction contained 125 points. The grid was discretized using a 2nd order central difference scheme (Eq. 6).

$$\nabla^2\phi_{i,j} = \frac{\phi_{i-1,j} - 2\phi_{i,j} + \phi_{i+1,j}}{\Delta x^2} + \frac{\phi_{i,j-1} - 2\phi_{i,j} + \phi_{i,j+1}}{\Delta y^2} \tag{6}$$

At the walls where there were no fixed (Dirichlet) boundary conditions, homogeneous von Neumann boundary conditions of $\nabla\phi = 0$ were enforced. At locations where there are Dirichlet boundary conditions they were enforced in a standard manner.

Once ϕ was determined at every grid point, the electric field was calculated from Eq. 7. The force per unit length was calculated from Lorentz's Law at each discretized volume in space (Eq. 8). For the purposes of implementing the force, it is desirable to leave the force in terms of force density (Eq. 9).

$$-\nabla\phi = E \tag{7}$$

$$F = -e(n_i - n_e)E\Delta x\Delta y\ [N/m] \tag{8}$$

$$f = -e(n_i - n_e)E\ [N/m^3] \tag{9}$$

The force in each direction was fit to a curve using MATLAB's curve fitting tool through non-linear regression. In order to provide an easily implemented forcing function, the force due to ions prior to the anode is disregarded when approximating the forcing function.

IV. Numerical Simulation of Flow

A. Overview of FDL3DI

FDL3DI is a 3D compressible Implicit Large Eddy Simulation (ILES) Navier Stokes solver with high order compact difference schemes[10]. FDL3DI performs its calculations in a rectangular numerical ξ, η, ζ domain which corresponds to the curvilinear body fit physical x, y, z domain. For brevity, the stencils will be explained in 1-D spatially and temporally. Let the domain be from 1 to N, where N is the ultimate point. Let M be the penultimate point. Consider an interior point i such that, $(i > 2 \| i < M) \& i \neq (1 \| N)$ (for 1,2, M, and N another stencil is used). For a scalar spatial derivative ϕ', it is defined by the tridiagonal system[10]:

$$\alpha\phi'_{i-1} + \phi'_i + \alpha\phi'_{i+1} = \beta\frac{\phi_{i+2} - \phi_{i-2}}{4} + \gamma\frac{\phi_{i+1} - \phi_{i-1}}{2} \tag{10}$$

The constants: $\alpha = \frac{1}{3}$, $\gamma = \frac{14}{9}$, and $\beta = \frac{1}{9}$, which are selected ensure sixth order accuracy. Similarly, the boundary conditions use high order formulations [10]. The inviscid flux derivatives are calculated by using Eq. 10. The viscous terms are then calculated using the primitive variables. High-order lowpass spatial filters are applied to avoid spurious components [10]. For a value ϕ, a filtered value, $\hat{\phi}$, is calculated using Eq. 11.

$$\alpha_f\hat{\phi}_{i-1} + \hat{\phi}_i + \alpha_f\hat{\phi}_{i+1} = \sum_{n=0}^{N}\frac{a_n}{2}(\phi_{i+n} + \phi_{i-n}) \tag{11}$$

The coefficient a_n is determined as a function of α_f from Ref. [10]. Currently the filter is set at $\alpha_f = 0.43$. This approach has been shown to be effective despite not using sub grid stress models[12][13]. An implicit approximately factored procedure is used to iteratively time march [12][13].

B. Numerical Setup

Because the forcing function obtained is two dimensional and the flow is in a 5 mm channel, the flow only was investigated in 2D. The Mach number was chosen to be 0.1 for numerical stability purposes[14]. The Mach number of 0.1 is essentially incompressible where the density variations will be extremely small within the domain. The Reynolds number was set to 3200. The Reynolds number was based on experimental values.

C. Grid and Boundary Conditions

The mesh was composed of 3 rectangular over set mesh regions that used a 5 point overlap to communicate. The two 'far field' meshes are identical, mirrored and overlapping with the channel region flow moving left to right. The grid uses a $y+ = 1.0$ near the flat plates. The mesh is vertically scaled near the wall with a $y+$ size which is then geometrically grown toward the center. The channel mesh has 658 points in the X direction and 1194 in the Y direction. The far field meshes on both sides have 443 points in the X direction and 848 Y direction. The reason for such a refined mesh is to capture the sharp force gradient near the wire. Along red lines (Fig. 4) at the wall, the no slip condition was enforced. Along blue lines, quiescent conditions were applied. The black lines indicated communication boundary conditions for overlapping meshes.

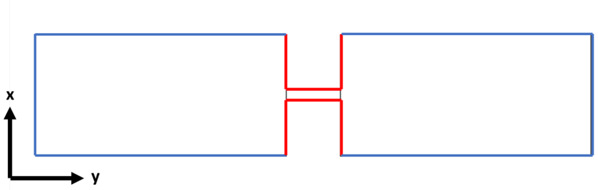

Fig. 4 A schematic of the simulation domain boundary conditions.

V. Results

A. Experimental Results

The PIV results indicated a mean flow of 4.23 m/s at the exit which was slightly lower than the reported result of 5 m/s by Campbell and Roy [3]. This difference was likely due to aforementioned variation in actuator construction and the fact that one side of the actuator tested in this paper was kept open for direct viewing inside the channel. The PIV result plotted in Fig. 5 shows recirculation regions just upstream of the inlet and stagnation region just downstream of the anode.

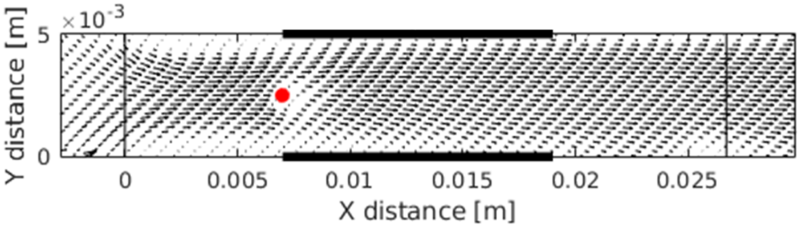

Fig. 5 Velocity vectors within the channel. The two vertical black lines represent the inlet and the outlet of the actuator. The red circle represents the anode and the horizontal black bars represent the cathode.

The streamwise velocity profile details plotted in Fig. 6 along four vertical lines show two distinct humps near the wire. The velocity profile then approaches slightly asymmetric fully developed flow pattern toward the outlet of the channel (Fig. 6).

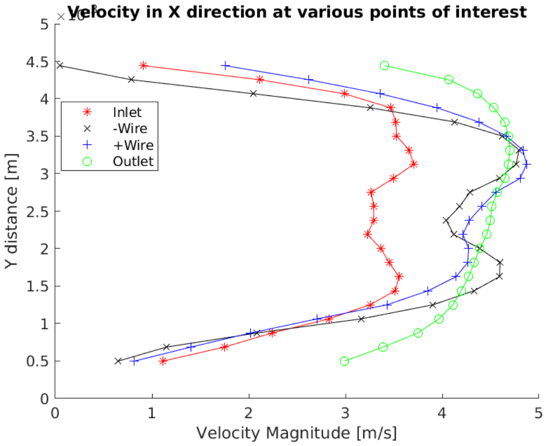

Fig. 6 Velocity profiles at various locations within the channel. Note the stagnation at the center which may be false data due to electromagnetic interference on the seeding[15]. The locations -Wire and +Wire indicate points 1 *mm* before the anode and 1 *mm* after the anode, respectively. The anode is 7 *mm* from the inlet.

B. Poisson Equation Results

Figure 7 shows the anticipated solution to the Poisson equation yielding a large concentration in the electric field near the wire. The resulting magnitudes of the force per unit depth of the channel follows the electric field peak about the wire and quickly decay as the distance from the wire increases (Fig. 8). The force again increases near the ground regions confirming a cathode sheath. Figure 9 shows the force in the X direction is concentrated near the wire and decays to zero. Figure 10 shows that most of the force in the Y direction is near the wire and quickly decaying to a constant force. The force in the Y direction is perfectly antisymmetric as expected. There is no force prior to the anode because it was assumed that the fluid prior to the anode was not ionized. This distribution of the x- and y- components of the electrostatic force was then fitted with an exponential forcing function similar to Singh and Roy [16] as shown in Eq. (12), (13). The coefficient of fit determination, R^2, for the force in the X direction was 0.996. The R^2 for the force in the Y direction was 0.898. The Y direction had sharper antisymmetric gradients near the anode making it more difficult to match. The parameter x_0 was the x position of the anode, y_0 was the y position of the anode, β is a decay rate constant and β_y is a growth constant specific to the y direction for the force in the y direction. The force function in the Y direction, F_y , is seen in Eq. 13. The constants are given in table 3. Both eqs. 12, 13 were simplified by reducing terms for ease of implementation.

$$F_x = F_{x0} e^{-\beta(|y-y_0|)-\beta(|x-x_0|)} \tag{12}$$

$$F_y = F_{y0} tanh(y - y_0) e^{\beta_y(|y-y_0|)-\beta(|x-x_0|)|} \tag{13}$$

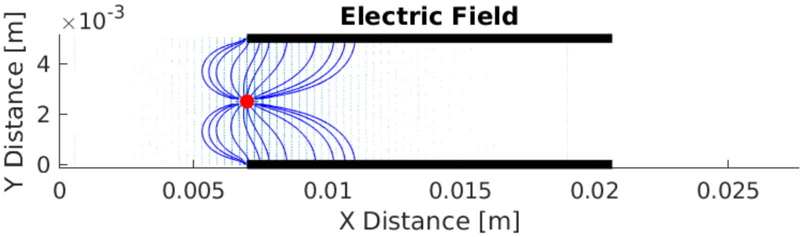

Fig. 7 The Electric field calculated from solving the Poisson equation. The red circle is the wire anode and the black bars are the ground cathodes.

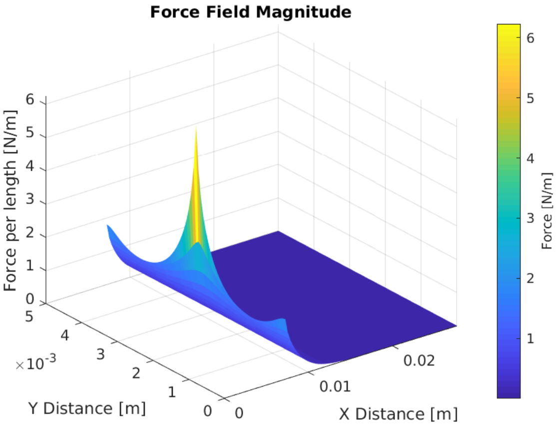

Fig. 8 The force field magnitude calculated from the Poisson equation shows majority force was near the wire.

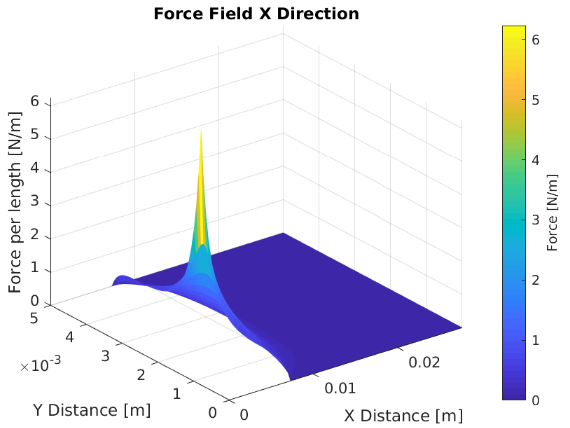

Fig. 9 The force field in the X direction calculated from the Poisson equation. Note the sharp gradient of the force around the wire.

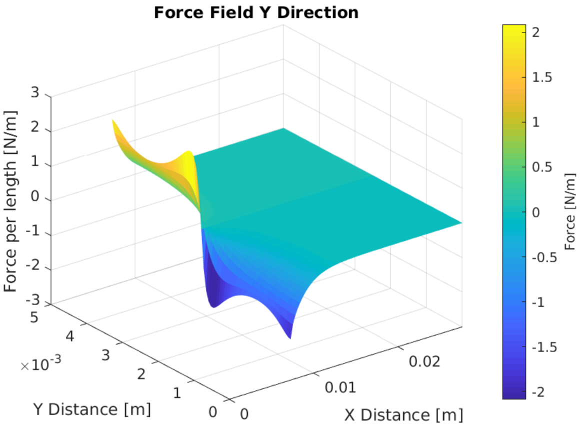

Fig. 10 The force field in the Y direction calculated from the Poisson Equation. Note the field is antisymmetric with a discontinuous jump at the anode location.

C. Numerical Simulation of Flow Results

As seen in Fig. 11, the computational flow was not stagnant downstream of the anode, whereas in Fig. 5 the PIV results from the flow experiment was stagnant in that region. However, the circulation regions upstream of the channel were similar to that in PIV shown in Fig. 5. The numerical and experimental velocity profiles at the inlet and outlet generally agree in both profile and velocity magnitude as seen in fig 6. The velocity from the simulation is approximately 1 m/s higher at the peak than the experimental results. This is expected as the experiment had one wall of the actuator open. Unlike the velocity profiles from the experiment, these profiles nearly obey continuity for an incompressible fluid

VI. Discussion

The recirculation in both experiment and simulation at the inlet (figs. 5,11) show potential for design optimizations. As seen in Fig. 7, there is a back force component of the flow which could be reduced by moving the anode farther from the cathode. The cost of moving the anode from the cathode is reducing the electric field by increasing the distance between anode and cathodes. The peak force in the Y direction is approximately half the value of the peak in the X direction (Fig. 9,10), which indicates that a third of the peak force is being wasted. The force in the Y direction is also mixing the high velocity flow at the center of the channel with low velocity flow near the wall further reducing efficiency.

Implementation of the forcing functions (eqs. 12, 13) can be made more accurate to capture force decay along the

Table 3 Parameters for the Forcing Functions

Symbol	Value/m	Value/m^3
F_{x0}	2.4 $[N/m]$	4.14e+07 $[N/m^3]$
F_{y0}	897 $[N/m]$	1.20E10 $[N/m^3]$
β	683 $[1/m]$	683 $[1/m]$
β_y	96 $[1/m]$	96 $[1/m]$
x_0	0.007 $[m]$	N/A
y_0	0.0025 $[m]$	N/A

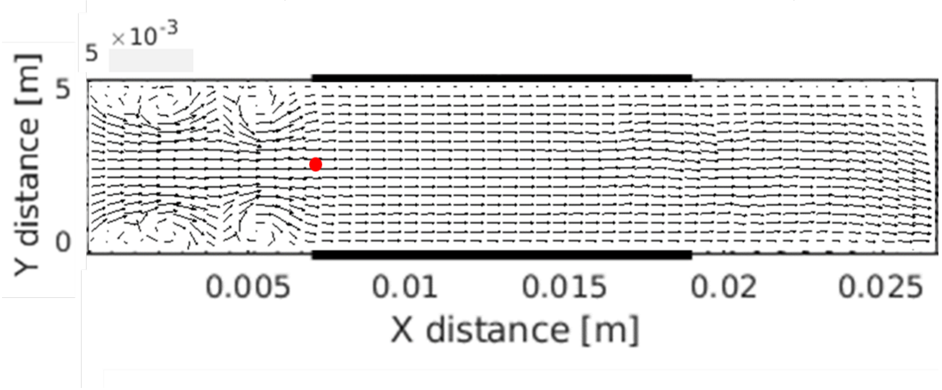

Fig. 11 The calculated velocity vectors show the flowfield inside the channel. The red circle represents the anode and the horizontal black bars represent the cathode. Note regions of recirculation at the upstream of the inlet and the lack of stagnation downstream of the wire.

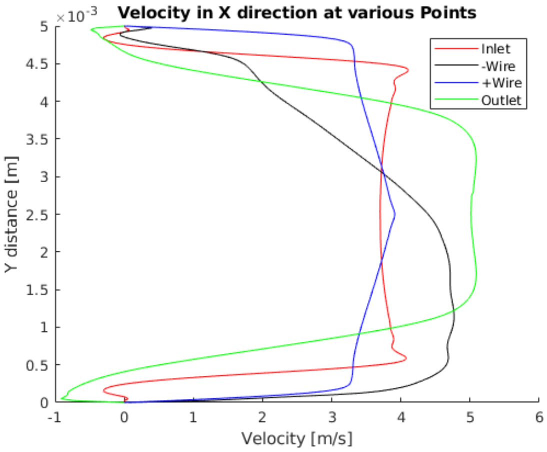

Fig. 12 Velocity profiles at various locations within the channel. Notice the profile becoming closer to fully developed. Note the lack of stagnation at the center. The locations -Wire and +Wire indicate points 1 *mm* before the anode and 1 *mm* after the anode, respectively. The anode is 7 *mm* from the inlet.

Debye length. The concern is that it would be necessary for the mesh to be refined to an extreme at the anode location, x_0,y_0 (Fig. 2), which may be undesirable for simulations that are significantly larger than the actuator. For unsteady simulations, the forcing function may have to be gradually increased up until its full force to avoid stability problems. More work could be done on finding a comparable force function that has a lower gradient which would reduce the need for a fine mesh, but could drastically reduce similarity of the experimental to simulation.

The averaged flow velocity profiles for both experiment and simulation nearly match at the inlet and exit (Fig. 12,5). As seen both flows have recirculation at the inlet. In figure 6, it appears that in the experiments the mean flow accelerates throughout the channel. According to Masati [15], for seeded plasmas with particles greater than 1350 nm of diameter, the particle showed velocity opposite to the flow. The seed used in this experiment was Ondina oil which yields particles between 1 and 5 μm. Unfortunately other seeding methods were not available for these experiments. It is hypothesized that as the oil particles approach the wire they are subject to both the drag of the flow pushing them and the electric field pushing them. Once they pass the anode they are pulled toward the anode by the electric force and pushed away from the anode by the drag of the flow. The push-pull phenomenon occurring between the electric field forces and air drag forces explains the apparent stagnation near the anode seen in fig 5.

The forcing function produced a flow quantitatively similar and qualitatively at the inlet and the outlet. Only near the anode did the simulation results and experimental results diverge (Fig. 12,6). As explained previously, this may be due to the seed reacting in an undesired manner when near the plasma (Masati [15]).

VII. Conclusions

By performing this research, we aim to deepen the understanding of the CDBD actuator, a niche but effective plasma actuator. This paper explored the simulation of plasma force using the Poisson-Boltzmann equation. Forcing functions were derived by approximately matching the numerical force vectors. The forcing function in the X direction is a constant multiplied by an exponential decay with a single decay constant. The force in the Y direction is a constant multiplied by a hyperbolic tangent with exponential decay in the X direction and exponential growth in the Y direction. The constant coefficients are determined by matching to the electrostatic force between the anode and cathodes. These functions were implemented into the FDL3DI solver and resulting flow simulation output were compared to the particle image velocimetry data. The major flow structures were characterized by reasonably matching the PIV results at the inlet and outlet and inside the channel. However, the forcing function did not match the PIV data just downstream of the wire. This may be due to seed moving counter to the flow due to the electrostatic field [15]. A full characterization of the effects of geometric parameters in Fig. 2 should be done.

The channel dielectric barrier discharge actuator could possibly see use in flow control where high velocity perturbations are needed or where a ’strong’ plasma pump is needed. An interesting extension to this work would be to compare the forcing function to time resolved particle image velocimetry. An interesting variation that may be explored is by using the same actuator but with semi bounded domain to enforce zero net mass flux. More work should be done on the effects of temperature on the flow as they can be used to increase actuator effectiveness. Future experiments may require seed much smaller than 1350 nm to completely validate this forcing function [17]. Further investigation must be done to understand the relationship between the PIV seed and plasma[15].

Acknowledgments

This work was partially supported by the AFRL funding through OAI-C2644-19296. The first author would like to thank Drs. Miguel Visbal, Daniel Garmann, and Caleb Barnes for lending their wisdom. The first author would also like to thank his labmates for their help. The first author would like to give thanks to the Graduate Student Preeminence Award (GSPA) at the University of Florida and the Student Stem Employment Program (SSEP) under the United States Air Force for funding support. This work was supported in part by high-performance computer time and resources from the DoD High Performance Computing Modernization Program.

References

[1] Wang, J. J., Choi, K. S., Feng, L. H., Jukes, T. N., and Whalley, R. D., “Recent developments in DBD plasma flow control,” *Prog. Aerosp. Sci*, Vol. 62, 2013, pp. 52–78.

[2] Roth, J. R., Sherman, D. M., and Wilkinson, S. P., “Boundary layer flow control with a one atmosphere uniform glow discharge surface plasma,” *AIAA Paper*, 1998, pp. 98–328.

[3] Campbell, N. S., and Roy, S., “Plasma channel flows: Electro-fluid dynamic jets,” *Applied Physics Letters*, Vol. 105, No. 13, 2014, p. 132906.

[4] Roth, J. R., Sherman, D. M., and Wilkinson, S. P., “Electrohydrodynamic flow control with a glow discharge surface plasma,” *AIAA journal*, Vol. 38, 2000, pp. 1166–72.

[5] Corke, T. C., Enloe, C. L., and Wilkinson, S. P., “Dielectric barrier discharge plasma actuators for flow control,” *Ann. Rev. Fluid Mech.*, Vol. 42, 2010, pp. 505–29.

[6] Gupta, A. D., and Roy, S., “Three-dimensional plasma actuation for faster transition to turbulence,” *J. Phys. D: Appl. Phys.*, Vol. 50, 2017, p. 425201.

[7] Durscher, R., and Roy, S., “Three-dimensional flow measurements induced from serpentine plasma actuators in quiescent air,” *J. Phys. D: Appl. Phys.*, , No. 45, 2012, p. 035202.

[8] Riherd, M., and Roy, S., “Measurements and simulations of a channel flow powered by plasma actuators,” *Journal of Applied Physics*, Vol. 112, 2012, p. 053303.

[9] Wang, C. C., and Roy, S., “Flow shaping using three-dimensional microscale gas discharge,” *Applied Physics Letters*, , No. 95, 2009, p. 081501.

[10] Gaitonde, D. V., and Visbal, M., “High-order schemes for Navier-Stokes equations: algorithm and implementation into FDL3DI,” , No. AFRL-VA-WP-TR-1998-3060, 1998.

[11] Thielicke, W., and Stamhuis, E., “PIVlab – Towards User-friendly, Affordable and Accurate Digital Particle Image Velocimetry in MATLAB,” *Journal of Open Research Software*, Vol. 1, No. 2, 2014, p. e30.

[12] Visbal, M., and Rizzetta, D., “Large-Eddy Simulation on Curvilinear Grids Using Compact Differencing and Filtering Schemes,” *Journal of Fluids Engineering*, , No. 124, 2002, pp. 836–847.

[13] Visbal, M., Morgan, P., and Rizzetta, D., “An Implicit LES Approach Based on High-Order Compact Differencing and Filtering Schemes,” *AIAA Paper*, 2003, p. 4098.

[14] Rizzeta, D. P., Visbal, M. R., and Morgan, P. E., “A high-order compact finite-difference scheme for large-eddy simulations of active flow control,” *JProg. Aerospace Sci*, Vol. 44, 2008, pp. 397–426.

[15] Masati, A., and Sedwick, R. J., “Electrostatic forces acting on particle image velocimetry tracer particles in a plasma actuator flow,” *Journal of Applied Physics*, , No. 123, 2018, p. 014904.

[16] Singh, K. P., and Roy, S., “Force approximation for a plasma actuator operating in atmospheric air,” *Journal of Applied Physics*, Vol. 103, 2008, p. 013305.

[17] Durscher, R., and Roy, S., “Evaluation of thrust measurement techniques for dielectric barrier discharge actuators,” *Exp Fluids*, 2011. https://doi.org/10.1007/s00348-012-1349-6.